INORGANIC CHEMISTRY FRONTIERS

RESEARCH ARTICLE

View Article Online
View Journal



Cite this: DOI: 10.1039/d5qi02269j

# Quantification of the synergetic contribution of a buried $WO_3/TiO_2$ heterojunction to photocatalytic activity

C. Sotelo-Vazquez, [a,b] R. Wilson,[c] R. Lee,[d] M. Ling, [c] S. Sathasivam, [e,f] R. Palgrave, [c] C. S. Blackman, [c] I. P. Parkin, [c] A. Iqbal, *[g] A. Kafizas *[h] and R. Quesada-Cabrera *[c,i]

The tungsten trioxide/titanium dioxide ($WO_3/TiO_2$) heterojunction is archetypical in photocatalysis, with demonstrated synergetic properties despite some controversy around the predominant band model in these systems. The current work is a systematic study that quantifies the synergetic contribution of a $WO_3/TiO_2$ heterojunction to the enhancement of photocatalytic activity over the contribution of a $TiO_2$ coating in core–shell nanostructures. The films were produced using atomic layer deposition and chemical vapour deposition techniques and their photocatalytic activity was correlated with transient absorption properties as a function of $TiO_2$ coating thickness. The study allowed the identification of an optimum thickness range within 21–40 nm, showing the greatest contribution of the heterojunction for a $TiO_2$ thickness of 30 nm. The outputs of this research have strong implications for heterojunction material design for practical applications.

Received 7th November 2025,
Accepted 23rd February 2026

DOI: 10.1039/d5qi02269j

rsc.li/frontiers-inorganic



## Introduction

Photocatalysts use light to drive a wide range of useful chemical transformations[1] and are increasingly being applied in commercial technologies, including self-cleaning windows,[2] concretes,[3] tiles[4] and paints.[5] The efficiency with which photocatalysts harvest and utilise light can be improved through rational material design strategies, with the use of heterojunction architectures becoming one of the most prominent strategies.[6]

Of the wide range of heterojunction photocatalysts studied to date, the tungsten trioxide/titanium dioxide ($WO_3/TiO_2$) heterojunction[7] has been demonstrated in numerous studies to exhibit synergistically higher activity than the sum of its parent materials,[8,9] and for the model organic pollutant degradation reaction – the mineralisation of stearic acid[10] – it has shown the highest activity among any thin film photocatalysts reported to date.[11] Therefore, $WO_3/TiO_2$ is now considered an archetypical system showing strong interfacial coupling and synergistic electronic properties.[12] Upon formation of a $WO_3/TiO_2$ heterojunction, the equilibration of Fermi levels results in interfacial band bending, which builds an internal electric field that promotes the separation of photogenerated charge carriers. Traditionally, this system has been described by a type-II band alignment model, with photogenerated electrons transferring from $TiO_2$ into the conduction band of $WO_3$ and positive holes migrating in the opposite direction. Previous work in our group,[8] combining hard X-ray photoelectron spectroscopy (HAXPES), transient absorption spectroscopy (TAS) and advanced hybrid density functional theory (DFT), challenged this model and proposed a band alignment that favoured the transfer of photogenerated electrons from $WO_3$ into $TiO_2$. Further studies using combined time-resolved computational studies and TAS confirmed that the charge transfer mechanism in the $WO_3/TiO_2$ heterojunction is dominated by the diffusion of excess electrons into $TiO_2$ and the transfer of

[a]Chemical and Environmental Engineering Group, ESCET, Universidad Rey Juan Carlos, C/Tulipán s/n, Móstoles, Madrid 28933, Spain
[b]Instituto de Investigación de Tecnologías para la Sostenibilidad, Universidad Rey Juan Carlos, C/Tulipán s/n, Móstoles, Madrid 28933, Spain
[c]Department of Chemistry, UCL (University College London), 20 Gordon St, London WC1H 0AJ, UK
[d]Department of Energy Conversion and Storage, Technical University of Denmark, Fysikvej, 2800 Kgs. Lyngby, Denmark
[e]School of Engineering & Design, London South Bank University, 103 Borough Road, London SE1 0AA, UK
[f]Energy, Materials & Environment Research Centre, London South Bank University, 103 Borough Road, London SE1 0AA, UK
[g]Materials Engineering, McGill University, 3610 University Street, Montréal QC H3A0C5, Canada. E-mail: asif.iqbal@mail.mcgill.ca
[h]Department of Chemistry, Imperial College London, The Molecular Science Research Hub, 82 Wood Lane, White City, London W12 0BZ, UK. E-mail: a.kafizas@imperial.ac.uk
[i]Department of Chemistry, FEAM-iUNAT, Universidad de Las Palmas de Gran Canaria, Campus de Tafira 35017, Las Palmas de Gran Canaria, Spain. E-mail: raul.quesada@ulpgc.es

holes over the valence band edge *via* thermionic emission in $WO_3$.[9] As the electrons are transported from $WO_3$ into $TiO_2$, a fully depleted $TiO_2$ coating allows electrons to be accommodated in the conduction band electron notch. This effect has a clear impact on the inhibition of electron–hole recombination, significantly increasing charge carrier lifetime. Meng *et al.*[13] pointed out that the accumulated photogenerated electrons in the conduction band of $TiO_2$ would reduce $O_2$ to a superoxide radical ($^{\bullet}O_2^-$) while photogenerated holes in the valence band of $WO_3$, with a more positive potential, could oxidize $H_2O$ (or $OH^-$ groups) to hydroxyl radicals ($^{\bullet}OH$). In a recent study,[7] some authors have proposed an S-scheme mechanism for $WO_3/TiO_2$ materials, where carriers with poor redox ability (respectively, electrons in the conduction band of $WO_3$ and holes in the valence band of $TiO_2$) recombine, thus promoting the separation of useful photogenerated carriers. More recently, Diez-Cabanes *et al.*[14] reported on the potential to tune band alignment at the $WO_3/TiO_2$ interface *via* morphological engineering.

A greater consensus has been reached over the clear enhancement of photocatalytic activity for $WO_3/TiO_2$ materials, although material engineering is still key for the optimisation of these systems for practical applications. Pinto *et al.*[15] recently carried out a systematic study of a heterojunction phase space in this system for photoelectrochemical water splitting, identifying regions of high, intermediate and low activity for a range of $WO_3$ nanorod lengths and $TiO_2$ coating thicknesses. Building on previous work, herein, we seek to quantify the impact of $TiO_2$ coating thickness on the observed synergetic increase in photocatalytic activity for a series of $WO_3/TiO_2$ heterojunction films. This is achieved by growing $WO_3$ nanorods of a fixed architecture (~30 nm in radial thickness and ~650 nm in length) and systematically coating them with a conformal layer of $TiO_2$, studying thicknesses from a few nanometers (~3 nm) to near microns (~500 nm) in length. High thickness control is achieved using atomic layer deposition (ALD), growing $TiO_2$ with thicknesses ranging from ~3 to ~110 nm. Thicker coatings were achieved using chemical vapour deposition (CVD), growing $TiO_2$ with thicknesses ranging from ~30 to ~500 nm. ALD and CVD are both gas-phase thin-film growth techniques, but with fundamentally different growth mechanisms. ALD relies on sequential, self-limiting surface reactions, which enables angstrom-level control over film thickness and highly uniform, conformal coatings even on complex, high-aspect-ratio nanostructures.[16] CVD involves continuous precursor supply and simultaneous gas-phase and surface reactions, offering less precise thickness control and reduced conformality, which can limit its effectiveness for nanoscale surface modification.[17] ALD is particularly effective for engineering surfaces and interfaces in photocatalytic systems, although the as-deposited films are often amorphous or weakly crystalline and they often require post-annealing. CVD uses high deposition temperatures, which favours faster growth and the formation of thicker, more crystalline films compared to ALD, resulting in good carrier mobility and long diffusion lengths for the promotion of photocatalytic performance.

The overall activity enhancement of the $WO_3/TiO_2$ films benefits from combined morphological and electronic components upon the construction of a high-surface area $TiO_2$-based photocatalyst and the heterojunction itself. Interestingly, we show how these effects essentially dissipate when the nanostructure of $WO_3$ is obscured through the coalescence of $TiO_2$ at a high coating thickness (*i.e.* ~500 nm), resulting in the loss of surface area and the localization of charge carriers in the material bulk where photocatalysis cannot occur. More importantly, from a balance of factors the optimum photocatalytic activity is seen at a critical $TiO_2$ coating thickness (*i.e.* at ~65 nm for films grown using ALD and at ~40 nm for those grown using CVD). These optima are quantified and rationalized using TAS and charge transport simulation methods.

## Experimental section

### Synthesis procedure

All chemicals were used as purchased from Sigma-Aldrich. $WO_3$ nanorods were deposited on quartz substrates (25 × 25 $mm^2$, Multi-Lab) using aerosol-assisted chemical vapour deposition (AACVD). Briefly, the precursor solutions were prepared using tungsten hexacarbonyl ($W(CO)_6$, 99%, $1.14 \times 10^{-2}$ M) in a 2 : 1 mixture of acetone (99%) and methanol (99.5%).[18] The dispersion was carried into the CVD reactor using an ultrasonic humidifier operating at 2 MHz (Liquifog, Johnson Matthey). The deposition was carried out at 350 ± 10 °C. The deposition of $WO_3$ nanorods was followed by deposition of $TiO_2$ films using either atomic layer deposition (ALD) or atmospheric-pressure chemical vapour deposition (APCVD). The APCVD films were deposited using titanium tetrachloride (99%) and ethyl acetate (99.8%) as metal and oxygen precursors, respectively.[12] Bubbler temperatures were set as 70 °C and 40 °C, at gas flow rates of 1.2 L $min^{-1}$ and 0.25 L $min^{-1}$, respectively. Film thicknesses were controlled by deposition time, ranging within 10–120 s. The deposition temperature was set to 500 °C. In ALD synthesis, $TiO_2$ films were produced from titanium(IV) isopropoxide (99.9%, TTIP) and water, using nitrogen as a carrier gas. The bubbler temperatures were set to 25 °C and 5 °C, at gas flow rates of 50 sccm and 0 sccm, respectively. The dose and purge times for TTIP were 2.5 s and 60 s, respectively. The dose and purge times for water were 2 s and 180 s, respectively. The purge lines in the system were set to 50 sccm. The deposition temperature for ALD $TiO_2$ films was set to 200 °C. Further details of the synthesis are given in the SI (Fig. S1–S4 and Table S1).

### Characterisation techniques

The morphology of the heterojunction films was explored using scanning and transmission electron microscopy (SEM/TEM) and atomic force microscopy (AFM). SEM was carried out using JEOL 6301 (5 kV) and JEOL JSM-6700F field emission instruments, equipped with a Hitachi S-3400 field emission instrument (20 kV) for energy-dispersive X-ray spectroscopy

 

(EDS) analysis. TEM images were collected using a high-resolution JEOL 2100 instrument, with a lanthanum hexaboride ($LaB_6$) source operating at an acceleration voltage of 200 kV. A Gatan Orius charge-coupled device (CCD) was used to acquire and record the micrographs. Each sample was prepared by scraping them off the quartz substrate using a diamond pen, followed by sonication in methanol, and dropcast onto a 400 Cu mesh lacy carbon film grid (Agar Scientific Ltd). AFM was performed using a Bruker Icon system running in PeakForce Quantitative Nanomechanical Property Mapping (QNM) mode. The topography of the samples was measured across 5 $\mu m^2$ areas using Bruker NCHV (etched silicon) tips in contact mode. The structural properties of the films were studied by X-ray diffraction (XRD) using a Bruker-AXS D8 (LYNXEYE XE) diffractometer with a copper (Cu) X-ray source ($K_{\alpha 1}$, $\lambda$ = 1.5406 Å) and at a glancing incident angle ($\theta$) of 1°. Each diffraction pattern was fit to the Le Bail method using structural parameters from the Joint Committee on Powder Diffraction Standards (JCPDS), through the GSAS and EXPGUI software suite. Micro-Raman spectroscopy was performed using a Renishaw 1000 spectrometer equipped with a 633 nm laser. This instrument was calibrated using a silicon reference. Optical UV/vis spectroscopy was carried out using a double monochromated PerkinElmer Lambda 950 UV/vis/NIR spectrophotometer, calibrated against a Labsphere reflectance standard. Transient absorption spectroscopy (TAS) was performed in diffuse reflectance mode, at a timescale range of 10 μs to 1 s. A Nd:YAG laser (OPOTEK Opolette 355 II, ~6 ns pulse width) was used as the excitation source, generating 355 nm UV light from the third harmonic. This laser light was transmitted to the sample *via* a liquid light guide. The laser was fired at a rate of 0.65 Hz and a power of ~1.2 mJ $cm^{-2}$. The probe light was generated from a 100 W Bentham IL1 quartz halogen lamp. Long pass filters (Comar Instruments) were placed to minimise short wavelength irradiation of the sample. Transient changes in absorption/diffuse reflectance from the sample were collected using a 2″ diameter, 2″ focal length lens and relayed to a monochromator (Oriel Cornerstone 130). The transient signal was measured at select wavelengths between 550 and 950 nm. Time-resolved intensity data were collected with a Si photodiode (Hamamatsu S3071). The data recorded at times $t$ > 3.6 ms were registered using an oscilloscope (Tektronics DPO3012) after passing the signal through an amplifier box (Costronics), whereas the data at $t$ < 3.6 ms were simultaneously recorded using a National Instrument DAQ card (NI USB-6251). Each kinetic trace was obtained from an average of 100–250 laser pulses. Acquisitions were triggered by a photodiode (Thorlabs DET10A) exposed to laser scatter. Data were acquired and processed using home-built software written in LabVIEW. Due to the nanostructured topography, all samples scattered light strongly and were thus measured in diffuse reflectance mode. As photo-induced changes in reflectance were low (<1%), it was fair to assume that the transient signal was directly proportional to the concentration of excited species. Much of the analysis herein considered the total transient absorption seen across these visible light wavelengths (550–950 nm) as a proxy for the total charge carriers present in the system at any given point in time.

### Photocatalytic testing

Photocatalytic screening was first carried out during the photodeposition of silver nanoparticles from a silver nitrate solution ($AgNO_3$, 0.5 M) under stirring conditions for 1.5 h, using a Vilber-Lourmat BLB lamp (2 × 8 W, $I$ = 3.15 mW $cm^{-2}$, $\lambda_{max}$ = 365 nm) as the light source. Further photocatalytic testing was assessed during the photodegradation of octadecanoic (stearic) acid, which was used as a model organic pollutant. A thin layer of stearic acid was dip-coated onto the films from a dispersion of the acid in chloroform (0.05 M). The degradation process was monitored *via* infrared spectroscopy (PerkinElmer RX-I). Further details are given in the SI.

## Computational section

A finite-difference (FD) numerical model was developed to investigate the electrostatic and charge-transport properties of the $WO_3/TiO_2$ heterojunction. The model self-consistently solves the coupled Poisson and carrier continuity equations (eqn. (1)–(3)), enabling a physically consistent description of band bending and carrier redistribution across the heterojunction. The theoretical framework closely replicates the experimental configuration, and full details of the numerical implementation have been reported in our previous work.[12,19]

$$\varepsilon \frac{d^2\phi}{dx^2} + \frac{d\phi}{dx}\frac{d\varepsilon}{dx} = -[Q_W + Q_T], \quad (1)$$

$$\frac{1}{q}\frac{dJ_n}{dx} + G_n - R_n = \frac{\partial n}{\partial t} = 0, \quad (2)$$

$$-\frac{1}{q}\frac{dJ_p}{dx} + G_p - R_p = \frac{\partial p}{\partial t} = 0. \quad (3)$$

Here, $\phi$ denotes the electrostatic potential across the heterojunction, while $Q_W$ and $Q_T$ represent the charge densities in $WO_3$ and $TiO_2$, respectively (subscripts "dark" and "light" indicate equilibrium and illuminated conditions). $J_n$ and $J_p$ are the electron and hole current densities, and n and p denote the spatially resolved electron and hole concentrations. Carrier generation terms $G_n$ and $G_p$ are calculated using the Lambert–Beer law, whereas electron and hole recombination (respectively, $R_n$ and $R_p$) is modelled *via* trap-assisted Shockley–Read–Hall processes. The spatial dependence of the dielectric constant $\varepsilon$ and grid discretization along the transport direction $x$ are explicitly accounted for. All material and transport parameters employed in the simulations are adopted from literature reports and summarized in Table S3 (SI).

## Results and discussion

A series of nanostructured $WO_3/TiO_2$ films (henceforth referred to as WTi-$L_T$, where $L_T$ as a number represents the

radial thickness in nanometers of the conformal $TiO_2$ layer grown on top of the $WO_3$ nanorods) was deposited using CVD ($30 \leq L_T$ (nm) $\leq 500$) and ALD methods ($3 \leq L_T$ (nm) $\leq 110$). Importantly, for this work, the growth conditions of the $WO_3$ nanorods were kept constant for all samples, with the rods having an average radial thickness of ~30 nm (Fig. S3). The resulting samples and their key properties are listed in Table 1. The use of two synthesis methods allowed for an evaluation of property trends independent of the synthesis approach, as well as enabling ultra-thin film growth using ALD (*i.e.* down to ~3 nm) and thicker film growth using CVD (*i.e.* up to ~500 nm). The deposition conditions in the case of the CVD synthesis were controlled to ensure the conformal coating of the nanorods. Microscopy images of the CVD films are shown in Fig. 1. As can be observed, short deposition times ($t$ < 15 s) resulted in the growth of separate $TiO_2$ particles on the $WO_3$ nanorods and were thus excluded from this study. However, a growth regime was established at longer deposition times ($15 \leq t$ (s) $\leq 60$) where conformal coating of the $WO_3$ nanorods occurred, with an average growth rate of *ca.* 1.7 nm $s^{-1}$ (Fig. S1). Further deposition times resulted in the coalescence of $TiO_2$ between neighbouring $WO_3$ sites, with the nanorods essentially buried beneath a thick coating of $TiO_2$ (herein deemed non-conformal, *nc*-WTi). The average $WO_3$ nanorod length was estimated at *ca.* 650 nm from the side-view SEM and TEM images (Fig. 1). AFM analysis accounted for the high surface roughness of the films, although surface roughness could not be adequately quantified using this technique. XRD and Raman spectroscopy confirmed the presence of monoclinic $WO_3$ and anatase $TiO_2$ phases (Fig. 2a and b). No evidence of other crystalline phases or metal mixing across the heterojunction boundary was observed, with unit cell volumes and crystallite sizes remaining constant for both phases upon deposition of the $TiO_2$ coatings (Fig. S6a and b). This was also confirmed by Raman spectroscopy (Fig. S6c), as the $E_g$ mode (symmetric stretching vibration of the O–Ti–O bonds), which is highly sensitive to metal doping, remained at 141 $cm^{-1}$ across the samples. Valence band (VB) spectra were fitted with $TiO_2$ and $WO_3$ models (Fig. 2c), following a methodology reported elsewhere.[21] Details of VB modelling are shown in Fig. S7. VB maxima for the parent material models were estimated at 3.21 eV and 2.72 eV, respectively for $TiO_2$ and $WO_3$, with a corresponding VBM offset of 0.49 eV. These values are consistent with those reported previously by HAXPES analysis and they confirmed the band model described in previous work.[10]

The formation of a $WO_3/TiO_2$ heterojunction had an impact on the surface reactivity of the films, as first evidenced by the photodeposition studies of Ag particles in a silver nitrate aqueous solution ($AgNO_3$, 0.5 M). Under similar experimental conditions, the size and shape of the photodeposited Ag particles can provide qualitative information on charge transfer and charge distribution events taking place at the film surface. As can be observed in Fig. 3, the conventional CVD $TiO_2$ film formed large, round Ag particles, as expected from an active photocatalytic semiconductor, with a conduction band of sufficient overpotential to effectively reduce $Ag^+$ ions. Instead, the $WO_3$ nanorods induced the formation of dendrite-like deposits, which can be associated with field enhancement effects at the tip of the nanorods, usually under non-equilibrium, diffusion-limited conditions.[21] The packed Ag deposits observed on the WTi heterojunction film suggested a combined mechanism for photodeposition, where large dendrites were formed likely due to an increase in electron density across the surface. It is worth noting, however, that the observation of this combined effect is not a *sine qua non* condition to demonstrate a synergistic interaction between the two semiconductors, since it could be due to the rod-like morphology of the $TiO_2$ layer in the film. Thus, further photocatalytic testing was carried out. Herein we explored the degradation of stearic acid, often used as a standard organic pollutant, deposited on the catalyst surface.[22] This approach follows the decay of characteristic C–H infrared bands of the acid under UV light (Fig. S8). The photocatalytic activity of the catalyst is estimated in terms of formal quantum efficiency, $\xi$, defined as molecules degraded per incident photon. The resulting $\xi$ values are plotted as a function of radial $TiO_2$ thicknesses, $L_T$, as shown in Fig. 4. Typical $\xi$ data from conventional $TiO_2$ films are consistent with the photon absorption properties of the films. The total light absorption at the peak irradiation wavelength of the photocatalysis experiment (*i.e.* 365 nm) across each WTi nanorod was calculated with knowledge of the absorption coefficient of $WO_3$ (~102 400 $cm^{-1}$)[23] and $TiO_2$ (~9900 $cm^{-1}$)[24] at this wavelength and thickness of each layer, assuming an average incident angle of light to each nanorod of 45° (Fig. S9). This followed a linear trend, with the absorbance increasing from ~58% in pure $WO_3$ to up to ~69% in WTi-110 (Fig. 4). Close inspection of the figure shows that WTi films with thin $TiO_2$ coatings ($L_T$ < 20 nm) had a near linear relationship between light absorption and photocatalytic activity; however, thicker $TiO_2$ coatings significantly deviated

**Table 1** Sample description of $WO_3/TiO_2$ heterojunction films (henceforth, WTi-$L_T$) synthesized from atomic layer deposition (ALD) and chemical vapour deposition (CVD), indicating corresponding average radial thicknesses for $WO_3$ ($L_W$) and $TiO_2$ ($L_T$), total light absorption, $A$ (%) and formal quantum efficiencies, $\xi \times 10^4$ (molecule/photon) with the average, $\langle x \rangle$, and standard deviation, $\sigma$, stated

| | | | | | $\xi \times 10^4$ (molecule/photon) | |
|---|---|---|---|---|---|---|
| Sample name | Method | $L_w$ (nm) | $L_T$ (nm) | $A$ (%) | $\langle x \rangle$ | $\sigma$ |
| WTi-3 | ALD | 30 | 3 | 58.41 | 0.33 | 0.02 |
| WTi-9 | ALD | 30 | 9 | — | 1.50 | 0.01 |
| WTi-13 | ALD | 30 | 13 | — | 2.25 | 0.02 |
| WTi-21 | ALD | 30 | 21 | 60.45 | 8.77 | 0.15 |
| WTi-30 | CVD | 30 | 30 | 61.44 | 10.82 | 0.29 |
| WTi-40 | CVD | 30 | 40 | 62.50 | 11.35 | 0.17 |
| WTi-65 | ALD | 30 | 65 | 65.04 | 10.01 | 0.07 |
| WTi-80 | CVD | 30 | 80 | 66.47 | 17.06 | 0.59 |
| WTi-110 | ALD | 30 | 110 | 69.18 | 10.37 | 0.12 |
| nc-WTi | CVD | — | 500 | 89.66 | 0.79 | 0.15 |

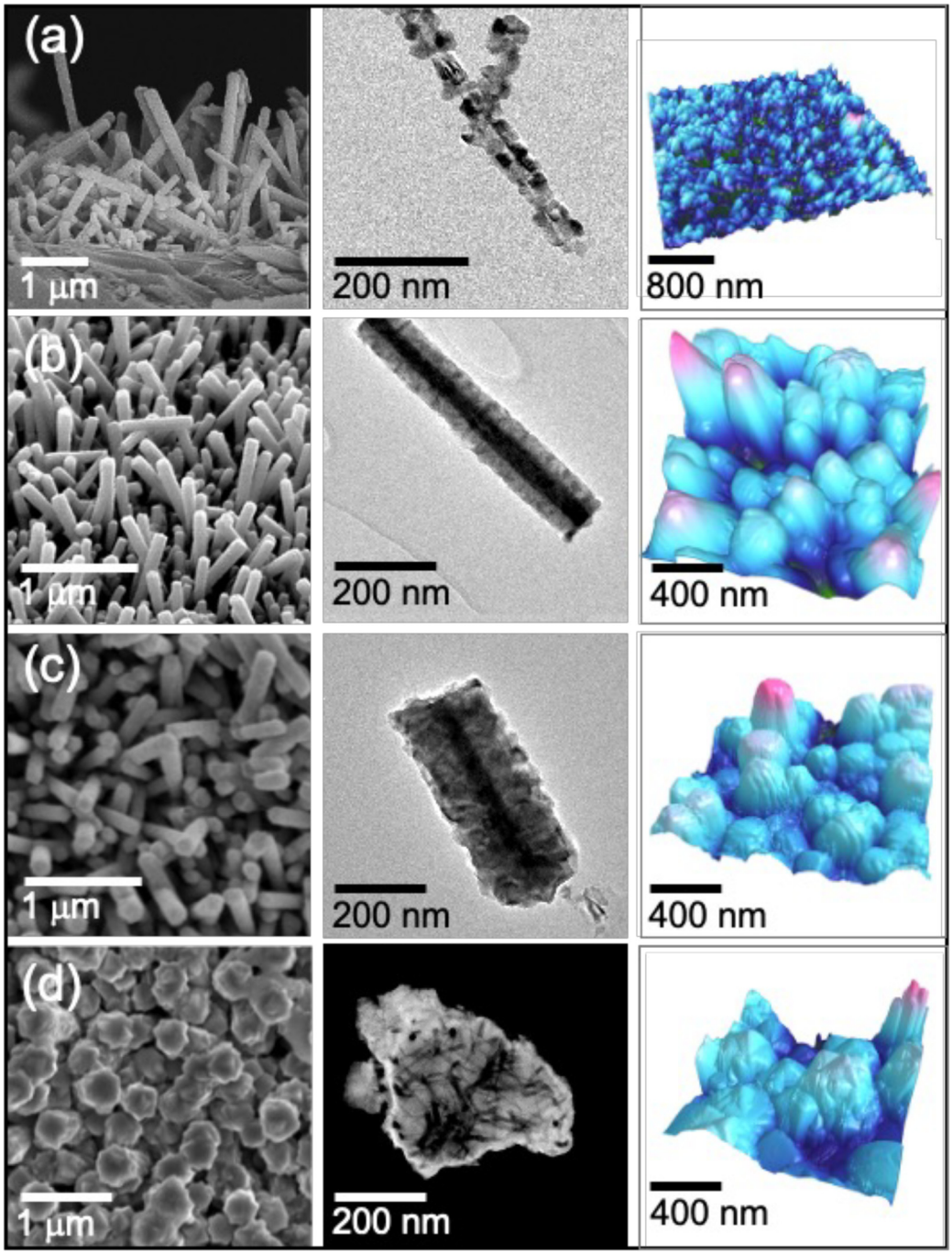


**Fig. 1** Microscopy images (respectively, SEM, TEM and AFM, from left to right) of selected heterojunction WTi films, obtained using $TiO_2$ deposition times of (a) 10 s, (b) 30 s, (c) 60 s and (d) 120 s, respectively. Corresponding average $TiO_2$ radial thicknesses within the conformally coated films were estimated as (b) $L_T$ = 30 nm and (c) $L_T$ = 80 nm, respectively. (d) Longer deposition times of $TiO_2$ films resulted in non-conformal coatings (*nc*-WTi).

from it, with films within $20 \leq L_T$ (nm) $\leq 40$ showing clear enhancements in photocatalytic activity with respect to the degree of light absorption. These enhancements were consistent, independent of the synthesis approach. Enhanced activity was also observed for the CVD WTi-80 film; however, other thick coatings produced by ALD (WTi-65 and WTi-100) resulted in comparatively lower activity, which was attributed to the differences in charge transport characteristics in the films prepared using each technique, where poorer crystallinity and charge transport were likely to be seen in $TiO_2$ layers deposited at the relatively low temperature of ALD (200 °C) compared to those deposited using CVD (500 °C). This is inferred upon inspection of XRD patterns of ALD $TiO_2$ films on glass substrates, as shown in Fig. S5.

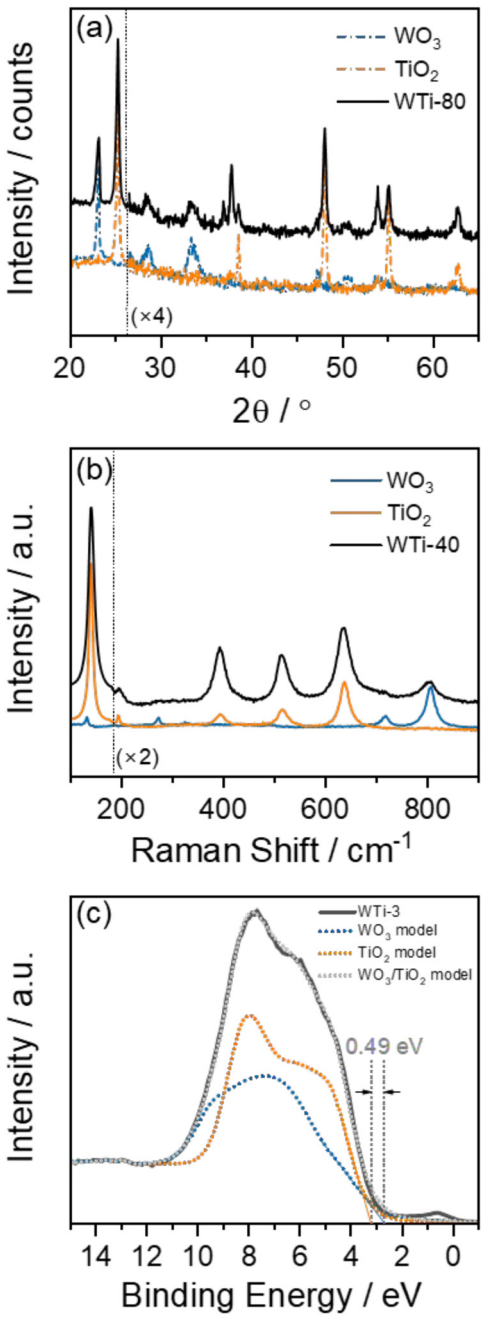


**Fig. 2** (a) Selected XRD patterns of the CVD sample WTi-80, including those of the parent materials. Peak intensities have been modified (×4) for $2\theta > 26.5°$ for clarity. (b) Raman spectrum of sample WTi-40, including the Raman spectra of the parent materials. Band intensities have been modified (×2) in the range above 180 $cm^{-1}$ for clarity. (c) Valence band (VB) spectra of sample WTi-3 fitted with VB models for $TiO_2$ and $WO_3$ components. The $TiO_2$ and $WO_3$ portions show only the model totals for each component for clarity. The VB fitting method is based on the approach previously reported for mixed phase $TiO_2$ systems.[20] The VB maximum offset (0.49 eV) of the fitted models is indicated.

The non-linear trend in photocatalytic activity seen in our series of WTi films can be explained using TAS, a technique which can measure the population and lifetime of charge carriers in $WO_3$,[25] $TiO_2$ [26] and their heterojunctions.[9] An example of TAS data is presented in Fig. S10 for the ALD WTi series. The transient decays probed at 550 nm show a dynamic that follows a power law function, which is typical of a thermally assisted trap-hopping recombination mechanism (Fig. S10a).[27] The transient absorption spectra showed broadband absorption, absorbing more prominently in the blue region (Fig S10b). The WTi-65 sample showed the highest degree of transient absorption at 1 ms and this indicated that this sample exhibited the highest number of charge carriers at this timescale in this series. Notably, it is from the 1 ms timescale that charge carriers can form reactive oxygen species that drive photocatalytic oxidation reactions,[1] and thus, to understand the photocatalytic activity trends observed herein, many of our comparisons below are made at this timescale. Importantly, significantly more charge carriers were present in the series of WTi heterojunctions compared with $TiO_2$ alone, which showed that the charge carrier formation, separation and lifetime were all higher in the heterojunctions, likely due to the formation of favourable band alignments and electric fields that promoted these effects; this is discussed in more detail later in this work.

As transient absorption in the visible region can be attributed to electron and hole carriers in both the $WO_3$ and $TiO_2$ components of the heterojunction, we used total transient absorption (from 550–950 nm) as a proxy for the charge carrier population at a given time. In Fig. S11 we show the total transient absorption at 1 ms after the laser pulse for the ALD and CVD WTi series, where within each series, the ALD WTi-65 and CVD WTi-40 films showed the highest degree of transient absorption. Importantly, many heterojunction samples in the series showed a synergistically higher level of transient absorption than the individual parent materials of which it was composed. This is informatively shown in Fig. 5, where the relative enhancements in charge carrier population either *vs.* its $TiO_2$ parent material or *vs.* the thinnest heterojunction produced, ALD WTi-3, are compared. Compared to the $TiO_2$ parent material, we used thick enough samples to maximise the optical absorption depth of $TiO_2$ while maintaining reasonable charge extraction to the surface, minimising charge transport limitations. A reasonable comparison (highest range) was thus set at thicknesses of 90 nm and 200 nm for ALD and CVD films, respectively. For the ALD series (Fig. 5a and b), the thinnest heterojunction, WTi-3, showed marginal enhancements in charge carrier population relative to a 90 nm thick ALD $TiO_2$ film, ranging from 2- to 5-fold enhancement. However, the growth of a 21 nm thick $TiO_2$ heterojunction, WTi-21, resulted in a substantial increase in charge carrier population from the 100 μs to 100 ms timescale, ranging from 10- to 40-fold enhancement. For the ALD series, the enhancements were highest in the WTi-65 sample, with a 40- to 50-fold increase relative to a 90 nm thick ALD $TiO_2$ film. For the CVD series (Fig. 5c and d), the greatest enhancements in transient absorption, relative to a 200 nm thick CVD $TiO_2$ film, were found in the 40 nm thick $TiO_2$ heterojunction, WTi-40, with a ~60-time increase seen at the

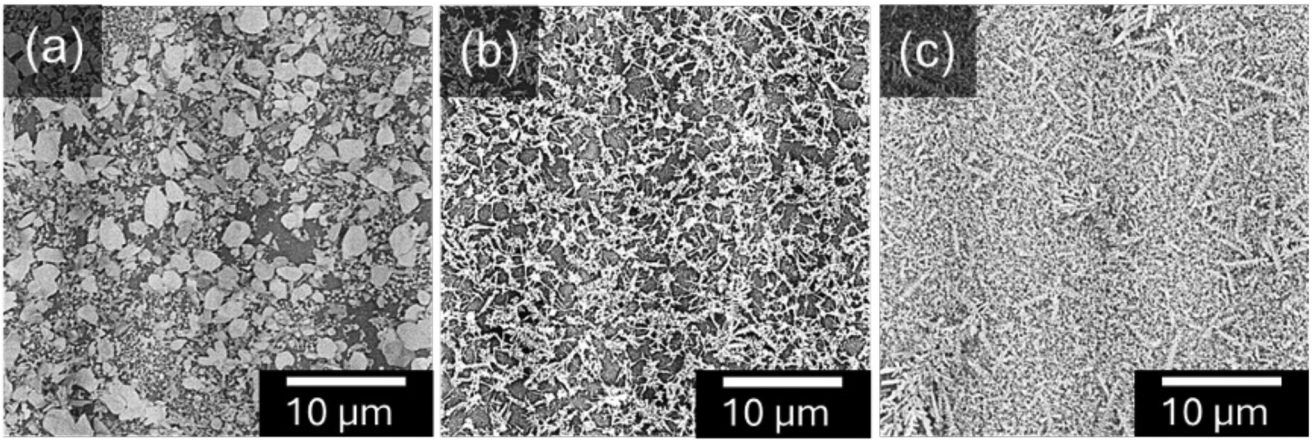


**Fig. 3** SEM images showing Ag particles photodeposited using an $AgNO_3$ solution (0.5 M) on: (a) a conventional CVD $TiO_2$ film; (b) a nanostructured $WO_3$ film; and (c) a heterojunction WTi film containing $TiO_2$-coated $WO_3$ nanorods.

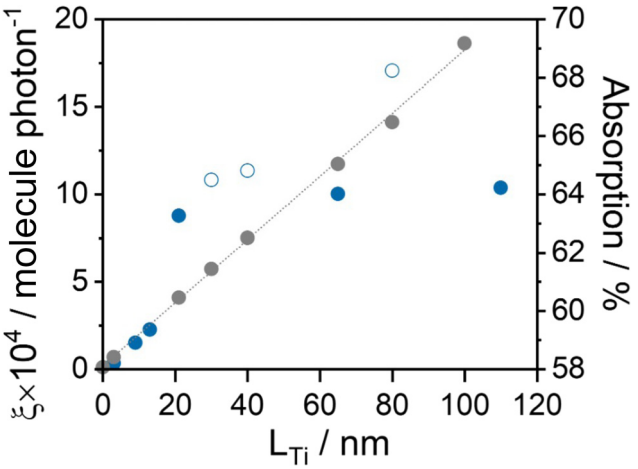


**Fig. 4** Formal quantum efficiencies, $\xi$ determined for ALD (full blue symbols) and CVD (empty blue symbols) WTi films. Total light absorption at 365 nm (grey symbols) – the irradiation wavelength of the photocatalysis experiment – was calculated with knowledge of the absorption coefficient of $WO_3$ (~102 400 $cm^{-1}$) and $TiO_2$ (~9900 $cm^{-1}$) at 365 nm and the thickness of each layer, assuming an average incident angle of light to each nanorod of 45°.

10 ms timescale. Overall, one can qualitatively see that the formation of a heterojunction results in up to a 60-fold increase in transient absorption, and thus charge carrier population, compared to $TiO_2$ alone (Fig. 5a and c), and that the formation of a heterojunction thicker than 3 nm $TiO_2$ (WTi-3) can result in an up to ~18-fold increase in transient absorption (Fig. 5b and d).

If we now plot the $TiO_2$ layer thickness in the WTi heterojunction against the total transient absorption (550–950 nm) at 1 ms after the laser pulse (Fig. 6a), this reveals a region of optimum layer thickness for the ALD and CVD series. For the ALD series, the maximum is observed at a $TiO_2$ thickness of 65 nm, and for the CVD series, the maximum is observed at a $TiO_2$ thickness of 40 nm. This indicates that the population of charge carriers at 1 ms – a timescale where the reactive oxygen species that drive a wide range of photocatalytic reactions can begin to form – is highest when the $TiO_2$ thickness in the heterojunction is between ~40 and 65 nm. Within this optimal region, charge carrier populations were several factors higher than those for $WO_3$ alone, and orders of magnitude higher than those for $TiO_2$ alone. Interestingly, when the $TiO_2$ thickness in the heterojunction was too high (*i.e.* 500 nm thick in *nc*-WTi), no enhancement was observed relative to $WO_3$ alone and only a marginal enhancement was seen relative to $TiO_2$ alone. This indicated that enhancements in charge carrier lifetime were not promoted in this structure, which may be attributed to the $TiO_2$ layer being too thick to facilitate effective charge transfer to the $WO_3$ core (and perhaps *vice versa*).

Now if we compare the $TiO_2$ layer thickness in the WTi heterojunction with photocatalytic activity (Fig. S12), we see a similar relationship to that of total transient absorption, with a maximum in photocatalytic activity being seen at a thickness of 65 nm. This showed that the total absorption at 1 ms (*i.e.* the charge carrier population) directly correlates with the observed photocatalytic activity, where a plot reveals a positive linear correlation ($r^2$ = 0.89) (Fig. 6b). Therefore, our transient absorption spectroscopy analysis showed that charge carrier populations and lifetimes are significantly enhanced in $WO_3$ and $TiO_2$ upon forming a $WO_3/TiO_2$ heterojunction, and that these enhancements in carrier populations map onto the observed photocatalytic activity with a high degree of correlation.

Finally, we also analysed the results from our computational models. Fig. 7 and 8 present the results of our numerical solution of the coupled Poisson and carrier continuity equations for the $WO_3/TiO_2$ heterojunction. Since both $WO_3$ and $TiO_2$ are intrinsically n-type, the interface constitutes an abrupt n–n isotype heterojunction, with electrons and holes acting as majority and minority carriers, respectively. Fig. 7a shows the computed equilibrium band diagram for a WTi-

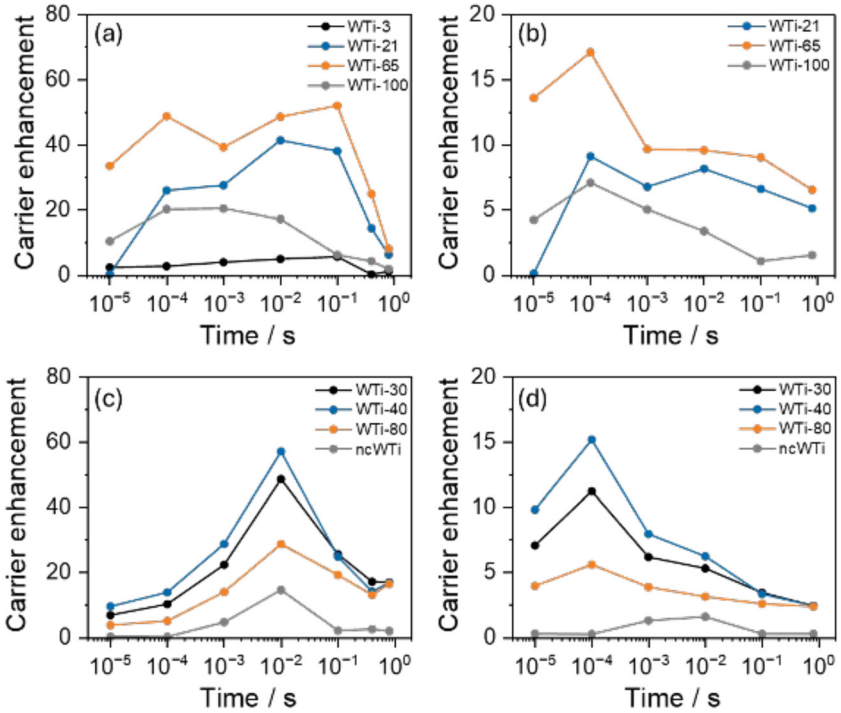


**Fig. 5** Relative carrier enhancements obtained from analysis of total transient absorption (550–950 nm) for ALD (top row) and CVD (bottom row) WTi films relative to single-phase $TiO_2$ (a and c) or WTi-3 (b and d) samples. The $TiO_2$ standards for ALD and CVD had thicknesses of 90 nm and 200 nm, respectively.

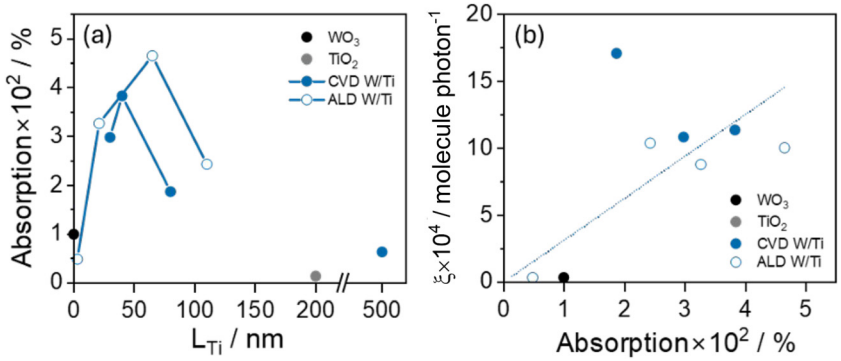


**Fig. 6** (a) Total transient absorption (550–950 nm, %) at 1 ms after the laser pulse as a function of $TiO_2$ thickness for the ALD and CVD WTi series, plotted alongside $WO_3$ and $TiO_2$ (200 nm thick CVD $TiO_2$) parent materials for comparison. Notably, the *nc*-WTi film shows similar behaviour to the 200 nm thick $TiO_2$ film. (b) A plot of the photocatalytic activity for the oxidation of stearic acid, $\xi$ (×$10^4$, molecules degraded per photon) against transient absorption (550–950 nm, %) at 1 ms after the laser pulse, showing a linear correlation, with a Pearson's correlation coefficient of 0.89.

65 heterojunction ($L_W$ = 30 nm; $L_T$ = 65 nm). Under dark equilibrium, a flat Fermi level ($E_F$) is established throughout the junction, confirming the absence of net current flow ($J$ = 0). Electron redistribution across the interface leads to the formation of a space-charge region ($SCR_{dark}$), which generates an internal electric field ($E_{field}$) across the heterojunction and plays a central role in governing charge separation under illumination, as discussed below. Upon UV illumination, photogenerated electron–hole pairs induce photovoltage ($V_{ph}$), as computed in Fig. 2b and c. Illumination results in (i) the splitting of the Fermi level into electron and hole quasi-Fermi levels ($E_{Fn}$ and $E_{Fp}$), and (ii) partial band flattening driven by $V_{ph}$.[12,19] The latter directly reduces the electrostatic barrier at the interface, thereby facilitating directional carrier transport across the heterojunction. Fig. 2c shows a comparison of the electrostatic potential profiles under dark ($V_{dark}$) and illuminated ($V_{light}$) conditions, revealing a band-flattening of approximately 59 meV.

To further elucidate the electrostatic and charge-transport characteristics of the WT heterojunction, we analyzed the

 

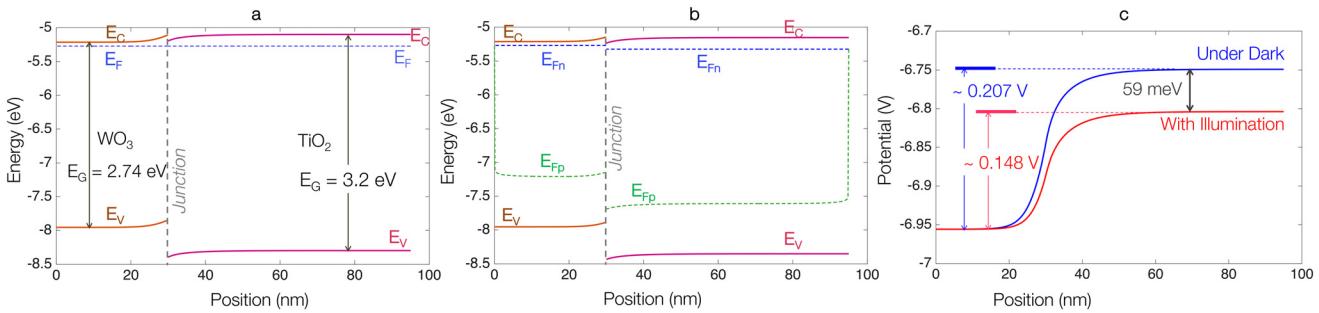


**Fig. 7** Calculated energy band diagrams of the WTi-65 heterojunction photocatalyst under (a) dark equilibrium and (b) UV illumination conditions. The $WO_3$ and $TiO_2$ layer thicknesses are $L_W$ = 30 nm and $L_T$ = 65 nm, respectively. The vacuum level in bulk $TiO_2$ under dark conditions is used as the reference potential (0 eV). Under equilibrium, the band diagram exhibits a flat Fermi level, a large valence-band barrier for hole transport, a small conduction-band barrier for electron transport, and distinct conduction- and valence-band discontinuities at the interface, characteristic of an abrupt n–n isotype heterojunction. Under UV illumination, the junction develops a photovoltage ($V_{ph}$), accompanied by splitting of the electron and hole quasi-Fermi levels. (c) Spatial profiles of the electrostatic potential under dark ($V_{dark}$, blue) and illuminated ($V_{light}$, red) conditions. Comparison of $V_{dark}$ and $V_{light}$ yields an illumination-induced band flattening of approximately 59 meV, which effectively acts as a forward bias and reduces the interfacial band bending.

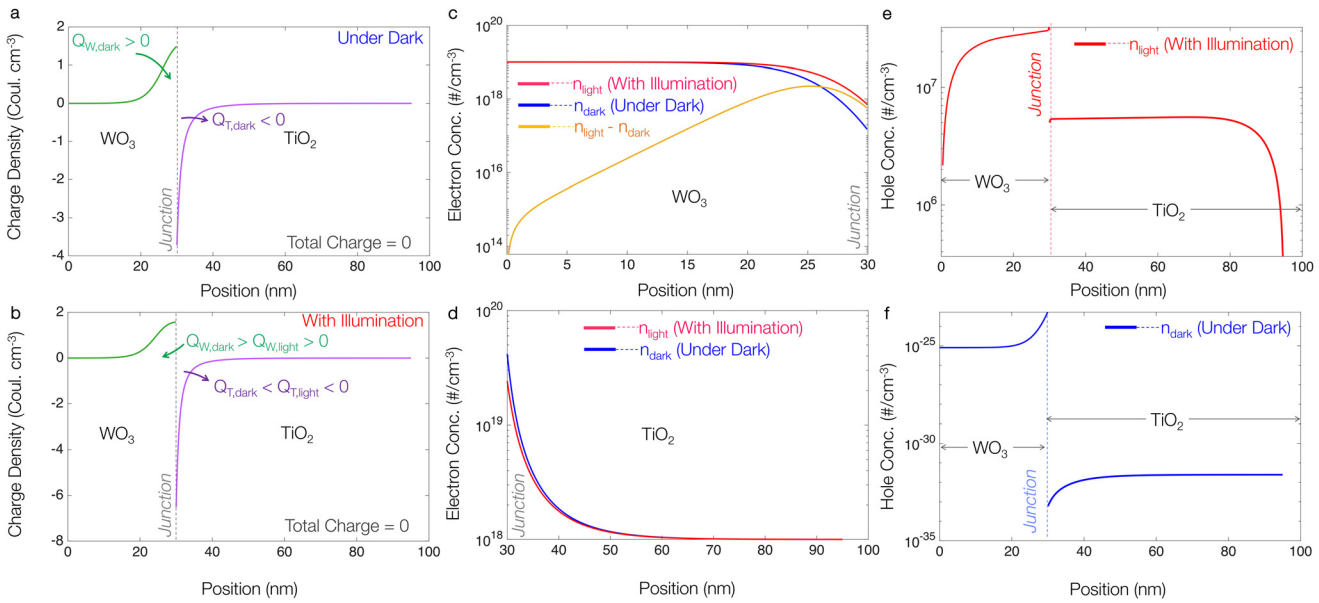


**Fig. 8** Calculated spatial distributions of net charge density across the WTi = 65 heterojunction under (a) dark equilibrium and (b) UV illumination. Under equilibrium, $WO_3$ exhibits a net positive space charge while $TiO_2$ exhibits a corresponding net negative space charge, arising from electron transfer from $WO_3$ to $TiO_2$ during Fermi-level equilibration. Upon UV illumination, the extent and magnitude of the space-charge region are reduced due to illumination-induced band flattening and the associated weakening of the internal electric field. (c) Accumulation of excess electrons on the $WO_3$ side of the junction (highlighted in yellow), obtained as the difference between electron concentrations under illumination ($n_{light}$, red) and dark conditions ($n_{dark}$, blue). (d) Spatial distributions of electron concentration in $TiO_2$ under dark ($n_{dark}$, blue) and illuminated ($n_{light}$, red) conditions. Spatial distributions of hole concentration along the heterojunction under (e) UV illumination and (f) dark conditions.

spatial evolution of the net charge density ($Q_W + Q_T$) along the transport direction. Fig. 8a and b show the calculated charge density profiles under dark equilibrium and 355 nm UV illumination, respectively. Under dark conditions, the $WO_3$ side exhibits a net positive space charge ($Q_{W,dark}$), while the $TiO_2$ side displays a corresponding net negative space charge ($Q_{T,dark}$). This charge separation originates from electron transfer from $WO_3$ to $TiO_2$ upon junction formation, consistent with Fermi-level equilibration. Charge neutrality is strictly preserved across the heterojunction, such that $Q_{W,dark} + Q_{T,dark} = 0$. Upon UV illumination, illumination-induced band flattening occurs as a result of photovoltage generation (Fig. 7c). This photovoltage effectively acts as a forward bias across the heterojunction, partially compensating for the built-in potential and reducing the overall band bending. Consequently, the space-charge region weakens. As shown in Fig. 8b, the net positive charge in $WO_3$ under illumination ($Q_{W,light}$) decreases relative to its dark value due to an increase in electron concentration within $WO_3$

(see Fig. 8c). Similarly, the magnitude of the net negative charge in $TiO_2$ ($Q_{T,light}$) is also reduced compared to $Q_{T,dark}$, reflecting a redistribution of carriers across the interface.

The illumination-induced modulation of carrier populations is quantified in Fig. 8c and d. Fig. 8c shows the accumulation of excess photogenerated electrons near the $WO_3$ side of the junction under illumination, while Fig. 8d reveals a reduction in electron concentration within $TiO_2$. This behavior is consistent with the downward shift of the electron quasi-Fermi level relative to the conduction-band minimum in $TiO_2$ (Fig. 7b). The corresponding hole concentration profiles (Fig. 8e and f) indicate negligible hole densities in the dark, as expected for n-type semiconductors, but substantial hole generation under illumination, with pronounced accumulation on the $WO_3$ side. This asymmetric hole distribution, together with the illumination-induced modulation of electron densities, promotes spatial separation of photogenerated charge carriers across the heterojunction, thereby suppressing recombination and enhancing the availability of charge carriers for surface reactions. We have analyzed the electrostatics and charge transport in great detail in our earlier work.[12]

To assess the influence of $TiO_2$ thickness on the electrostatic response of the WT heterojunction, we solved the coupled Poisson and carrier continuity equations (eqn (1)–(3)) for variable $TiO_2$ thickness ($L_T$), while maintaining a fixed $WO_3$ thickness of $L_W$ = 30 nm. The resulting electric-field profiles are shown in Fig. 9. As $L_T$ increases from 20 to 80 nm, the $TiO_2$ surface progressively moves away from the buried heterojunction, leading to a significant attenuation of the electric field at the surface. For example, in the WTi-65 configuration, the electric-field strength within $TiO_2$ drops below 1% of its interfacial maximum beyond ~42.8 nm from the interface. In the case of WTi-20, although the $TiO_2$ layer is fully depleted, its limited thickness restricts optical absorption and photocarrier generation, preventing effective utilization of photocarriers generated in the $WO_3$ layer. However, an optimal balance between optical absorption, photocarrier generation, and electric-field-driven charge separation is achieved for $L_T \approx 30$ nm. For thicker $TiO_2$ layers, the influence of the interfacial electric field diminishes, and photocatalytic activities increasingly arise from the intrinsic properties of $TiO_2$ and the nanostructured, high-surface-area morphology of the film rather than from heterojunction-driven charge separation.

The results obtained from this study can be summarised in Fig. 10. The overall efficiencies of the WTi samples resulted from two contributions: (a) the individual, nanostructured $TiO_2$ coatings and (b) the $WO_3/TiO_2$ heterojunction synergy. The samples with relatively thin $TiO_2$ coatings (WTi-21, WTi-30 and WTi-40) take advantage of the synergetic effect, showing unusually high quantum efficiencies, while those with thick coatings (WTi-80) mainly benefit from the individual $TiO_2$ nanostructure. This is in line with our previous work,[11] which identified an optimum $TiO_2$ thickness of $L_T \approx 30$ nm for an effective charge separation towards promoting photocatalytic activity at the WTi interface. It also aligns with the optimum length scales of 10–20 nm reported for bulk heterojunctions.[28] Considering the average diffusion lengths of electrons and holes in anatase $TiO_2$,[29] the minority carriers (*e.g.* holes) have much shorter diffusion lengths (typically 10 nm) compared to the majority carriers (*e.g.* electrons), which are typically within 1–10 μm. This means that the photocatalytic activity is largely restricted by the transport of hole carriers, hence aligning with the optimum length scales observed in practice. Notably, the formation of a heterojunction can induce electric fields that

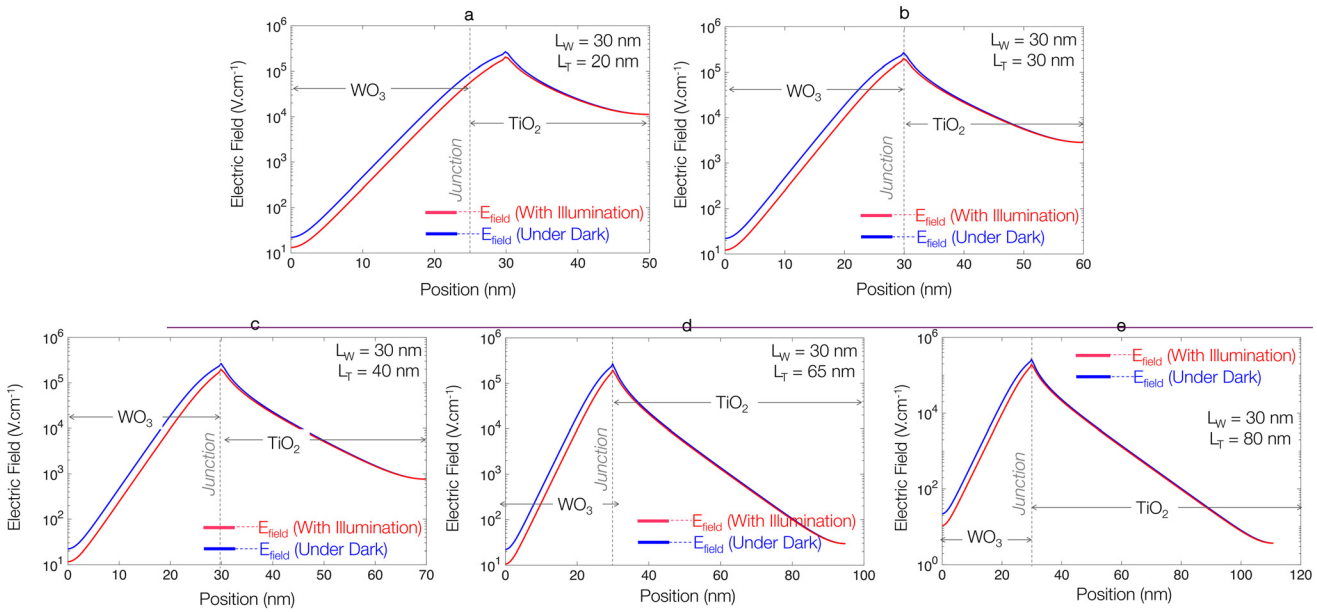


**Fig. 9** Calculated spatial distribution of the electric field of the $WO_3/TiO_2$ heterojunction with $L_W$ is 30 nm and (a) $L_T$ = 20 nm, (b) $L_T$ = 30 nm, (c) $L_T$ = 40 nm, (d) $L_T$ = 65 nm and (e) $L_T$ = 80 nm.

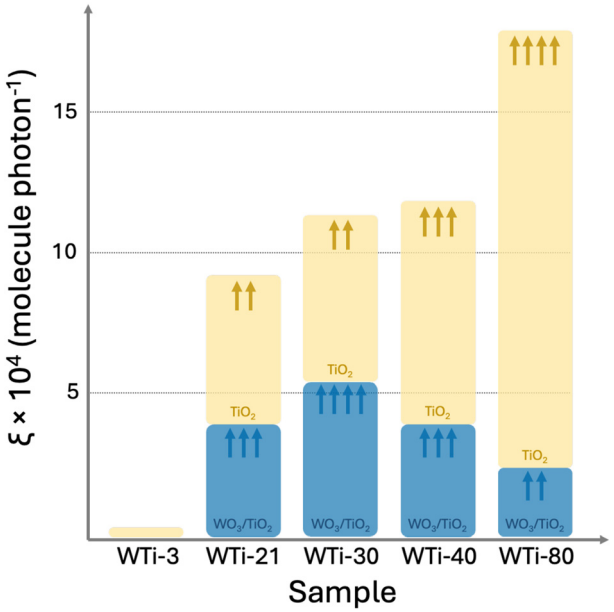


**Fig. 10** Schematic figure illustrating contributions from the nanostructured $TiO_2$ coatings (yellow bars) and the buried $WO_3/TiO_2$ heterojunctions (blue bars) in selected samples (namely WTi-3, WTi-21, WTi-30, WTi-40 and WTi-80). The arrows refer to relative contributions within the two types: WTi-30 shows the greatest benefit from the $WO_3/TiO_2$ heterojunction while WTi-80 benefits particularly from $TiO_2$ thickness and individual photocatalytic properties.

can drive band bending, thus promoting more favourable hole carrier transport and average diffusion lengths well beyond 40–50 nm, as evidenced from this work.

## Conclusions

A series of nanostructured $WO_3/TiO_2$ films was deposited using CVD and ALD methods, with radial thicknesses of $TiO_2$ coatings ranging between 3 and 110 nm. The photocatalytic activity of these films was studied during degradation of a standard organic pollutant (stearic acid) and their quantum efficiencies correlated with their respective transient absorption properties, particularly those within meaningful reaction timescales. Deviation from the trend in photon absorption and relative carrier enhancements observed from transient absorption spectroscopy allowed for the quantification of the $WO_3/TiO_2$ heterojunction contribution within the overall quantum efficiency. Significant contributions were particularly observed within films containing thin $TiO_2$ coatings within 21–40 nm, with an optimum thickness of 30 nm, which showed the greatest benefit from the synergetic effect between the two semiconductors. On the other hand, the formation of the heterojunction is less relevant in films with relatively thick $TiO_2$ coatings (80 nm), which mainly benefit from the nanostructured (*i.e.* high surface area) nature of the film and the individual photocatalytic properties of $TiO_2$. These contributions may represent a trade-off in material design for practical applications, particularly when it comes to scalability and industrial use. In particular, given that the optimal material can be produced by CVD, which is a technique used to grow $TiO_2$ photocatalysts at scale for self-cleaning glazing applications, the approach introduced in this work is inherently of industrial relevance.

## Conflicts of interest

There are no conflicts of interest to declare.

## Data availability

The data supporting the findings of this study are available within the article and its supplementary information (SI). The SI includes schematics of our CVD apparatus, SEM images of $TiO_2$ layer thickness as a function of deposition time, EDS cross-sections of our $WO_3/TiO_2$ heterojunctions, ALD synthesis conditions and AFM images of $TiO_2$ coatings grown using ALD, XRD analysis and Le Bail refinment, VB analysis using XPS of exemplar $WO_3$ and $TiO_2$ samples, details on our photocatalytic testing protocol using a model pollutant stearic acid, details of our light absorption model and graphical data, transient absorption kinetics and spectra of select samples, a plot of formal quantum efficiency of stearic acid degradation against $TiO_2$ layer thickness, and calculation parameters for our computational modelling. See DOI: **https://doi.org/10.1039/d5qi02269j**.

Additional raw data, including transient absorption spectra, photocatalytic degradation measurements, and simulation outputs, are available from the corresponding author upon reasonable request.

## Acknowledgements

R.Q.C. thanks the Spanish Ministry of Science and Innovation (MCI) and the Next Generation EU/PRTR Programme for grant PID2022-143294OB-I00. A.K. thanks the EPSRC for a Programme Grant (EP/W017075/1). C.S.V. would like to thank the Regional Government of Madrid for financial support through Programa de Atracción de Talento "César Nombela" 2023 (2023-T1/ECO-29048). I.P.P. thanks EPSRC grant EP/L015862/1 for support.

## References

1 A. Fujishima, X. Zhang and D. A. Tryk, $TiO_2$ photocatalysis and related surface phenomena, *Surf. Sci. Rep.*, 2008, **63**, 515–582; K. Hashimoto, H. Irie and A. Fujishima, $TiO_2$ photocatalysis: A historical overview and future prospects, *Jpn. J. Appl. Phys.*, 2005, **44**, 8269–8285.

2 A. Mills, A. Lepre, N. Elliot, S. Bhopal, I. P. Parkin and S. A. O'Neill, Characterisation of the photocatalyst

Pilkington Activ™: a reference film photocatalyst?, *J. Photochem. Photobiol., A*, 2003, **160**, 213–224.

3 Y. Zhang, Y. Zhou, X. Dong, X. Xi and P. Dong, Recent advances in $TiO_2$-based photocatalytic concrete: Synthesis strategies, structure characteristics, multifunctional applications, and CFD simulation, *Chem. Eng. J.*, 2024, **496**, 154186.

4 P. São Marcos, J. Marto, T. Trindade and J. A. Labrincha, Screen-printing of $TiO_2$ photocatalytic layers on glazed ceramic tiles, *J. Photochem. Photobiol., A*, 2008, **197**, 125–131.

5 Th. Maggos, J. G. Bartzis, M. Liakou and C. Gobin, Photocatalytic degradation of $NO_x$ gases using $TiO_2$-containing paint: A real scale study, *J. Hazard. Mater.*, 2007, **146**, 668–673.

6 J. Low, J. Yu, M. Jaroniec, S. Wageh and A. A. Al-Ghamdi, Heterojunction photocatalysts, *Adv. Mater.*, 2017, **29**, 1601694; H. Wang, L. Zhang, Z. Chen, J. Hu, S. Li, Z. Wang, J. Liu and X. Wang, Semiconductor heterojunction photocatalysts: Design, construction, and photocatalytic performances, *Chem. Soc. Rev.*, 2014, **43**, 5234.

7 N. M. Makwana, R. Quesada-Cabrera, I. P. Parkin, P. F. McMillan, A. Mills and J. A. Darr, A simple and low-cost method for the preparation of self-supported $TiO_2$–$WO_3$ ceramic heterojunction wafers, *J. Mater. Chem. A*, 2014, **2**, 17602–17608; R. Quesada-Cabrera, E. R. Latimer, A. Kafizas, C. S. Blackman and I. P. Parkin, Photocatalytic activity of needle-like $TiO_2/WO_{3-x}$ composite thin films prepared by atmospheric pressure chemical vapour deposition, *J. Photochem. Photobiol., A*, 2012, **239**, 60–64.

8 F. He, A. Meng, B. Cheng, W. Ho and J. Yu, Enhanced photocatalytic $H_2$-production activity of $WO_3/TiO_2$ step-scheme heterojunction by graphene modification, *Chin. J. Catal.*, 2020, **41**, 9–20.

9 J. Y. Lee and W.-K. Jo, Heterojunction-based two-dimensional N-doped $TiO_2/WO_3$ composite architectures for photocatalytic treatment of hazardous organic vapor, *J. Hazard. Mater.*, 2016, **314**, 22–31; Q. Wang, W. Zhang, X. Hu, L. Xu, G. Chen and X. Li, Hollow spherical $WO_3/TiO_2$ heterojunction for enhancing photocatalytic performance in visible-light, *J. Water Process Eng.*, 2021, **40**, 101943.

10 A. Mills and J. Wang, Simultaneous monitoring of the destruction of stearic acid and generation of carbon dioxide by self-cleaning semiconductor photocatalytic films, *J. Photochem. Photobiol., A*, 2006, **182**, 181–186; R. Fretwell and P. Douglas, An active, robust and transparent nanocrystalline anatase $TiO_2$ thin film – preparation, characterisation and the kinetics of photodegradation of model pollutants, *J. Photochem. Photobiol., A*, 2001, **143**, 229–240; S. Alofi, C. O'Rourke and A. Mills, Photocatalytic destruction of stearic acid by $TiO_2$ films: Evidence of highly efficient transport of photogenerated electrons and holes, *J. Photochem. Photobiol., A*, 2003, **435**, 114273; P. Evans, S. Mantke, A. Mills, A. Robinson and D. W. Sheel, A comparative study of three techniques for determining photocatalytic activity, *J. Photochem. Photobiol., A*, 2007, **188**(2–3), 387–391.

11 C. Sotelo-Vazquez, R. Quesada-Cabrera, M. Ling, D. O. Scanlon, A. Kafizas, P. K. Thakur, T.-L. Lee, A. Taylor, G. W. Watson, R. G. Palgrave, J. R. Durrant, C. S. Blackman and I. P. Parkin, Evidence and effect of photogenerated charge transfer for enhanced photocatalysis in $WO_3/TiO_2$ heterojunction films: A computational and experimental study, *Adv. Funct. Mater.*, 2017, **27**, 1605413.

12 A. Iqbal, A. Kafizas, C. Sotelo-Vazquez, R. Wilson, M. Ling, A. Taylor, C. Blackman, K. Bevan, I. P. Parkin and R. Quesada-Cabrera, Charge transport phenomena in heterojunction photocatalysts: The $WO_3/TiO_2$ system as an archetypical model, *ACS Appl. Mater. Interfaces*, 2021, **13**, 9781–9793.

13 S. Meng, W. Sun, S. Zhang, X. Zheng, X. Fu and S. Chen, Insight into the transfer mechanism of photogenerated carriers for $WO_3/TiO_2$ heterojunction photocatalysts: Is it the transfer of band–band or Z-scheme? Why?, *J. Phys. Chem. C*, 2018, **122**, 26326–26336.

14 V. Diez-Cabanes, A. Morales-Garcia, F. Illas and M. Pastore, Tuning the interfacial energetics in $WO_3/WO_3$ and $WO_3/TiO_2$ heterojunctions by nanostructure morphological engineering, *J. Phys. Chem. Lett.*, 2021, **12**, 11528–11533.

15 F. Pinto, A. Wilson, B. Moss and A. Kafizas, Systematic exploration of $WO_3/TiO_2$ heterojunction phase space for applications in photoelectrochemical water splitting, *J. Phys. Chem. C*, 2022, **126**, 871–884.

16 S. M. George, Atomic layer deposition: An overview, *Chem. Rev.*, 2009, **110**(1), 111–131.

17 K. L. Choy, Chemical vapour deposition of coatings, *Prog. Mater. Sci.*, 2003, **48**(2), 57–170.

18 M. Ling and C. Blackman, Growth mechanism of planar or nanorod structured tungsten oxide thin films deposited via aerosol assisted chemical vapour deposition (AACVD), *Phys. Status Solidi C*, 2015, **12**(7), 869–877.

19 A. Iqbal and K. H. Bevan, Simultaneously solving the photo-voltage and photocurrent at semiconductor–liquid interfaces, *J. Phys. Chem. C*, 2018, **122**, 30–43.

20 R. Lee, R. Quesada-Cabrera, J. Willis, A. Iqbal, I. P. Parkin, D. O. Scanlon and R. G. Palgrave, Phase Quantification of heterogeneous surfaces using DFT simulated valence band photoemission spectra, *ACS Appl. Mater. Interfaces*, 2023, **15**, 39956–39965.

21 K. G. M. Laurier, M. Poets, F. Vermoortele, G. De Cremer, J. A. Martens, H. Uji-i, D. E. De Vos, J. Hofkens and M. B. J. Roeffaers, Photocatalytic growth of dendritic silver nanostructures as SERS substrates, *Chem. Commun.*, 2012, **48**, 1559–1561.

22 A. Mills and J. Wang, Simultaneous monitoring of the destruction of stearic acid and generation of carbon dioxide by self-cleaning semiconductor photocatalytic films, *J. Photochem. Photobiol., A*, 2006, **182**, 181–186; S. Alofi, C. O'Rourke and A. Mills, Study and modeling of the kinetics of the photocatalytic destruction of stearic acid islands on $TiO_2$ films, *J. Phys. Chem. C*, 2023, **127**, 12194–12205.

 

23 A. Kafizas, L. Francas, C. Sotelo-Vazquez, M. Ling, Y. Li, E. Glover, L. McCafferty, C. Blackman, J. Darr and I. P. Parkin, Optimizing the activity of nanoneedle structured $WO_3$ photoanodes for solar water splitting: Direct synthesis via chemical vapor deposition, *J. Phys. Chem. C*, 2017, **121**, 5983–5993.

24 A. Kafizas, Y. Ma, E. Pastor, S. R. Pendlebury, C. Mesa, L. Francas, F. Le Formal, N. Noor, M. Ling, C. Sotelo-Vazquez, C. J. Carmalt, I. P. Parkin and J. R. Durrant, Water oxidation kinetics of accumulated holes on the surface of a $TiO_2$ photoanode: A rate law analysis, *ACS Catal.*, 2017, **7**, 4896–4903.

25 S. Corby, L. Francas, A. Kafizas and J. R. Durrant, Determining the role of oxygen vacancies in the photoelectrocatalytic performance of $WO_3$ for water oxidation, *Chem. Sci.*, 2020, **11**, 2907–2914.

26 A. Kafizas, X. Wang, S. R. Pendlebury, P. Barnes, M. Ling, C. Sotelo-Vazquez, R. Quesada-Cabrera, C. Li, I. P. Parkin and J. R. Durrant, Where do photogenerated holes go in anatase:rutile $TiO_2$? A transient absorption spectroscopy study of charge transfer and lifetime, *J. Phys. Chem. A*, 2016, **120**, 715–723.

27 B. Moss, K. K. Lim, A. Beltram, S. Moniz, J. Tang, P. Fornasiero, P. Barnes, J. Durrant and A. Kafizas, *Sci. Rep.*, 2017, **7**, 2938.

28 A. J. Hegger, *Adv. Mater.*, 2014, **26**, 10–28.

29 T. Luttrell, S. Halpegamage, J. Tao, A. Kramer, E. Sutter and M. Batzill, *Sci. Rep.*, 2014, **4**, 4043.